THE FABRY-PEROT INTERFEROMETER ON DYNAMICS EXPLORER

P. B. HAYS, T. L. KILLEEN, and B. C. KENNEDY
Space Physics Research Laboratory, University of Michigan, Ann Arbor, MI 48109, U.S.A.

(Received, 20 April 1981)

Abstract. The Fabry-Perot Interferometer (FPI) on Dynamics Explorer is a remote sensing instrument designed to measure the temperature, meridional wind and density of the metastable atoms $O(^1S)$ and $O(^1D)$ and the ion $O^+(^2P)$ in the thermosphere. The measurements are made with a stable, high resolution Fabry-Perot etalon, which performs a wavelength analysis on the light detected from the thermospheric emission features by spatially scanning the interference fringe plane with a multichannel array detector. The wavelength analysis characterizes the Doppler line profile of the emitting specie. A sequential altitude scan performed by a commandable horizon scan mirror provides a cross-sectional view of the thermodynamic and dynamic state of the thermosphere below the orbit of the Dynamics Explorer 'B' satellite.

1. Introduction

The Fabry-Perot Interferometer (FPI) on the Dynamics Explorer is a highly stable single etalon interferometer containing the optics to view the Earth's atmosphere at various tangent heights. The information obtained from a single instrumental spectral and spatial scan will allow us to discern the temperature, meridional wind and density of any one of several excited atoms or ions in the thermosphere. Thus, by using a series of such observations we can provide a cross sectional view of the thermodynamic and dynamic

TABLE I

FPI measurements

Species	Spectral region	Scientific value
$O(^1D)$	6300 Å	Thermal line, upper thermosphere neutral wind and temperature.
$O^+(^2P)$	7320 Å	Thermal line, upper thermospheric ion drift and temperature. Non-thermal line, oxygen corona and ion velocity distribution at high field strengths.
$O(^1S)$	5577 Å	Thermal line, mesospheric nighttime neutral winds and lower thermospheric daytime. Non-thermal line, nighttime thermosphere.
$N(^2D)$	5200 Å	Thermal line, auroral energy storage.
$Na(^2P)$	5896 Å	Thermal line, mesospheric neutral wind and temperature daytime.

Space Science Instrumentation **5** (1981) 395–416. 0377–7936/81/0054–0395 $03.30.

state of the thermosphere below the orbit of the Dynamics Explorer 'B' spacecraft. The specific excited species utilized in our observations are listed in Table I along with a few comments on the geophysical conditions under which these emission features will be utilized. We note that the morphology of many of these emission features has been extensively investigated with the Visible Airglow Experiment on the Atmosphere Explorer spacecraft series [1]. A consequence of this knowledge is the ability to select the emission feature which will be most useful in a particular study of thermospheric dynamics.

1.1. Scientific objectives

The principal goal of the experimental investigation discussed here is to provide the Dynamics Explorer Science Team cross-sectional views of the dynamic and thermodynamic state of the thermosphere below the spacecraft at all times that such information is desired. These data when combined with the important information concerning ion and neutral composition, zonal ion and neutral winds, particle energy deposition, and electric and magnetic fields provided by other investigators will allow us to address the central problems associated with the dynamic state of the thermosphere.

The scientific problem of primary interest to this investigation is to understand how the heat deposited in the thermosphere is ultimately dissipated, through wind systems and conductive transport. It is well known at this time that there are three primary sources of thermospheric energization, these being solar extreme ultraviolet radiation, magnetospheric energy either as particle or joule heating near the magnetic poles, and wave or tidal energy transported upward through the lower boundary. However, although these sources are known, their relative contributions are in doubt and the time history of polar heating related to magnetic storms is still not well understood. Not only do the uncertainties about the energy sources and the dynamic transport of energy exist, but the influence of potential energy storage in the form of composition variations, both inert and chemically active, is not well defined. These problems are well discussed in the reviews of [2], [3], and [4]. The principal reason for these uncertainties is the lack of accurate morphological data on the wind and temperature fields.

1.2. Instrument requirements

The present state of knowledge concerning the dynamics of the thermosphere is sufficient to define very clearly the requirements of future measurements. The amplitude of the variance of the temperature from the global mean is of the order of 10%, that is about 100 K [2]. Similar values are observed in the polar regions [5]. Thus we desire a measure of temperature that is at least one order of magnitude better than this. The main diurnal neutral wind fields have amplitudes of about 50 m s^{-1}, whereas the polar winds during magnetic storms can exceed this number by a factor of 10. Therefore, we desire a knowledge of the wind field to about ± 5 m s^{-1}.

These desired measurements determine the spectral properties of this instrument. The spectral width of the instrument should approximately match the thermospheric line width and should exhibit environmental shifts of less than that produced by a 5 m s^{-1} doppler shift. Furthermore, it is useful to select the instrumental period (Free Spectral

Range) to equal the doppler shift created by the satellite motion. These requirements are summarized below:

1. Free Spectral Range 0.156 Å
2. Instrument Width 0.016 Å
3. Stability $\pm 1.0 \times 10^{-4}$ Å.

The optical scanning characteristics of the instrument are determined by the desire to view the horizon over a 200 km vertical region below the satellite orbit, to sample that region in steps which do not exceed the local scale height and to perform the measurements in a reasonable time period. These desires are achieved within the constraints imposed by the need to baffle the instrument against sunlight by limiting the scan to the angular region from 5 to 15 deg below the local horizon and by dividing the horizon into two sets of 8 elements, each scanned in 12 s, a rate corresponding to modest oversampling of the horizon.

We note that the directional bias limits our measurements during half of the mission when the spacecraft, for thermal control purposes, is oriented such that the FPI field of view points away from the horizon.

2. Instrument Description

2.1. Optics

The Fabry-Perot interferometer has a field of view of 0.53 deg (semi-cone angle) defined by a doublet objective lens and a field stop. The view direction with respect to the spacecraft is selected by a convex mirror which may be commanded to perform a sequential scan or to remain at any preselected position. There are 24 scan mirror positions, 16 of which correspond to view directions varying between 5 and 15 deg below the spacecraft $+X$-axis. The minimum dwell time for each step of a sequenced horizon scan is 0.5 s, and two full, 8 step, horizon scans (one scanning up and one down) are accomplished for each rotation of the cam. In addition to selecting the view direction, the scan mirror has two calibration positions to enable the instrument to view one of two atomic line discharge lamps or a calibration source of phosphor activated by radioactive Promethium[147].

Figure 1 shows an optical schematic for the Fabry-Perot interferometer. The cone of light rays defined by the main objective, scan mirror and field stop is collimated by a three element collimator telescope of focal length 15.8 cm. The beam then passes through two blockers, a filter wheel containing eight filters and the high resolution etalon. For an extended monochromatic source, the etalon produces an interference ring pattern at infinity. This pattern is localized in the plane of the detector photocathode by a folded refractive telescope of focal length 0.78 m.

All optical elements, with the exception of the higher refractive index components of the collimator and the etalon objective telescope, were made from BK7 G-25, radiation resistant glass. The other two elements were made from radiation resistant SF6 G-5 glass. The optical design was fully raytraced and carefully optimized to minimize the

off-axis blurring due to optical aberrations. Because of the long effective focal length required for the etalon objective telescope and the need to keep the overall instrument size manageable, it was not possible to use diffraction limited optics throughout. However, the instrument maintains a spot size of less than 100 μ (circle of least confusion) to 0.5 deg off axis.

2.2. Main scanning telescope and baffle

The main objective telescope consists of a doublet lens with an oval mask to define its working area. The lens forms a real image of the sky on the sky stop. This image is reduced by the stop to a vertical slice of the horizon and the scan mirror selects circular elements, corresponding to different view directions, for analysis by the interferometer.

The purpose of the main baffle is to eliminate stray light which enters the optics from the bright limb of the earth or the sun. To limit the size of the baffle while maintaining a large horizon scan angle, the system has been designed to form a real image of the scan mirror in the plane of the critical baffle located near the center of the main baffle tube. All selected input light beams thus pivot about a point defined by the critical baffle and the instrument axis. In other aspects the two-stage baffle is similar to that flown in the Visible Airglow instrument on Atmosphere Explorer [1] with an improved performance due to use of the Martin Marietta blacking process on internal surfaces. The entire baffle system is protected against contamination by dust particles up to and during launch by a cover with a quartz window. This cover is retained by a biphenyl latch mechanism which releases in orbit.

2.3. Fabry-Perot interferometer

The central component of the instrument is the etalon which performs the high resolution spectral analysis by multiple path interference of the transmitted light. The etalon consists of two fused silica substrates upon each of which is deposited a semi-reflecting dielectric multilayer. These mirrors are flat to 1/100 of a wavelength and are held apart and parallel by three Schott 'Zerodur' spacing elements. The spacer end surfaces are cemented to the etalon plates using a UV-curable anaerobic adhesive (Rees 1980, Private communication). The operating parameters of the interferometer are listed in Table II.

The spectral information is in the form of a modified Airy function with argument:

$$\frac{2\mu_0 d_0}{\lambda_0}\left(1 + \frac{\delta d}{d_0} - \frac{\delta\lambda}{\lambda_0} - \frac{\theta^2}{2}\right),$$

where

d_0 = the separation of the two semi-reflecting surfaces;
μ_0 = the refractive index of the medium in the etalon gap (in orbit = 1.0);
λ_0 = the center wavelength at resonance on axis;
δd = a variation in d about d_0;
θ = the angle of the light path through the etalon relative to the normal.

It can be seen that a change in wavelength is associated with a change in plate separation d and also with a change in θ. The FPI uses a technique for measuring changes

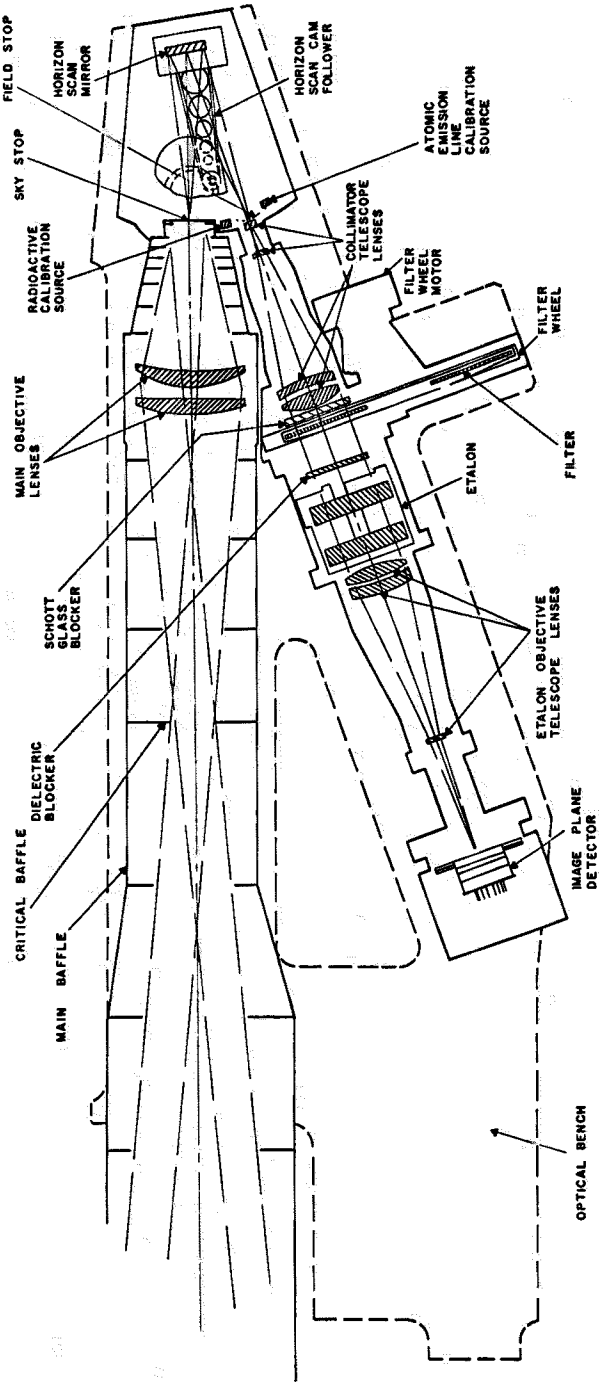

Fig. 1. Optical schematic for the Fabry-Perot Interferometer.

TABLE II

Parameters of interferometer

1. Etalon plates	
effective diameter	3.3 cm
unconstrained flatness	$\lambda/100$
reflective coatings	five alternative layers ZnS and MgF2 with 1% overcoat of MgF_2
reflectivity	0.81 at 6300 Å
reflective finesse	14.9
spacing	1.26 cm
2. Etalon Objective telescope	
effective focal length	78.2 cm
3. Interferometer field of view	0.44 deg
4. Free Spectral Range	0.157 Å (6300 Å)
5. Detector	
anode structure	12 concentric ring, equal area anodes.
photocathode	S 20
total working aperture	1.2 cm diam
dark count at 12 °C	12 Hz/anode
spectral range per anode	0.016 Å (6300 Å)
6. Interference filters	
center wavelength/ half bandwidth:	6300/10 Å
	6300/40 Å
	5577/10 Å
	5577/3 Å
	7320/10 Å
	7320/10 Å
	5896/10 Å
	5200/10 Å
7. Overall working finesse at 6300 Å:	
ch1: 8.15	
ch2: 6.23	
ch3: 5.96	
ch4: 5.70	
ch5: 5.58	
ch6: 5.53	
ch7: 5.36	
ch8: 5.36	
ch9: 5.25	
ch10: 5.30	
ch11: 5.30	
ch12: 2.82	
8. Temperature stability	
To measurement of wind:	41.5 m s^{-1}/°C
wavelength stability:	0.00087 Å/°C
9. Knowledge of Etalon temperature	0.02 °C

in wavelength involving detection and quantification of changes in the angle θ of the resonantly transmitted light. This technique employs a novel, photon counting, multi-channel Image Plane Detector (see next section).

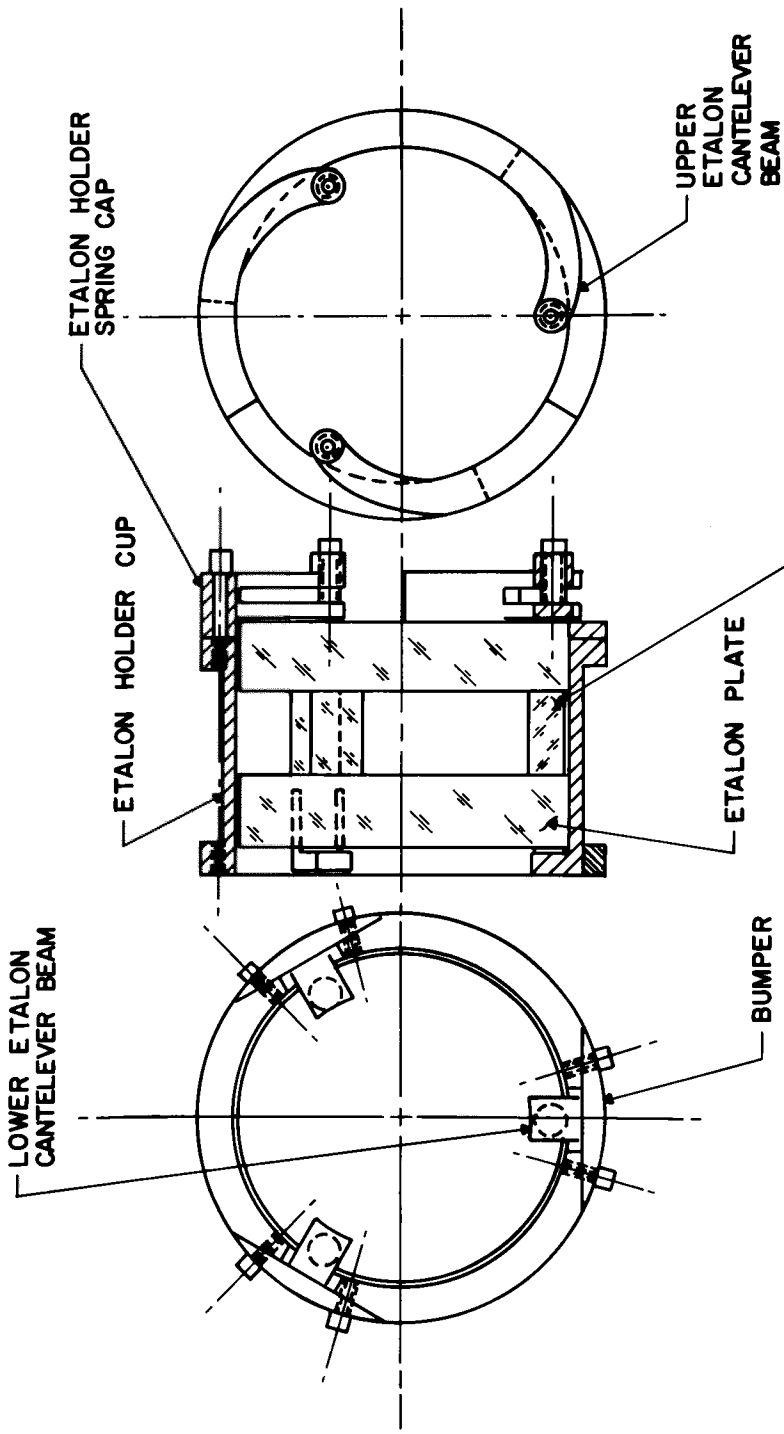

Fig. 2. Schematic of etalon mounting arrangement.

The stability requirement for the measurement of winds of the order of $10\ m\ s^{-1}$ requires that the etalon plate separation, d, be stable to 1.0×10^{-7} cm. ($d_0 = 1.26$ cm). To satisfy this requirement the material of the etalon spacers was selected from a batch of the glass ceramic 'Zerodur' having a thermal expansion coefficient of 2.0×10^{-8} cm/cm-K. Also, the etalon has been protected from distortions due to changes in the thermal environment by use of a kinematic mount made of Invar. In this design the etalon is epoxied at six places to the end pads of the elastic cantelever beam springs shown in Figure 2. The spring constants have been chosen such that the incremental forces on the etalon due to thermally induced changes in the mount are small enough to preclude appreciable elastic compression or expansion of the spacing material.

The interferometer section comprising etalon, objective telescope and detector is thermally insulated from the instrument baseplate. This is achieved by mounting the section between two thin, (150 μ), stainless steel diaphragms. The interferometer section is gold plated and is covered, but not contacted, by a radiation shield which is also gold plated to avoid temperature gradients acros the plates due to the radiative transfer of thermal energy to and from the etalon block.

2.4. Image Plane Detector

The Image Plane Detector (IPD) is the electro-optical device that converts the intensity distribution of light falling on the image plane into a set of discrete electron pulses. The output pulses from each of 12 anodes are counted by the instrument electronics over an integration period of 0.22 s for every 4 minor frames, that is every 0.25 s.

A schematic diagram of the IPD, which was developed by ITT, Electro-Optical Products, is shown in Figure 3(a). The device has a 12 mm effective diameter face plate on which an extended red (S20) photocathode is deposited. Behind the photocathode is a three-stage, microchannel plate (MCP) electron multiplier operating at a gain of 10^6. The output of the multiplier is collected on a segmented anode composed of 12 concentric, equal area ring elements. The anode is situated within 0.26 mm of the output plane of the MCP to avoid serious defocusing of the interference ring pattern. Figure 3(b) shows the layout of the anode; the IPD is masked to prevent illumination of those areas of the photocathode corresponding to the output leads of the individual ring anodes.

The geometrical parameters of the anode are tabulated in Table III. Since the anodes are of equal area, they each monitor an equal interval of the wavelength spectrum.

The imaging properties of the IPD have been studied using a travelling spot probe. The broadening function due to the IPD electron optics is estimated, by gaussian deconvolution, to be approximately 55 microns FWHM for all channels. A second characteristic broadening function arises from the fact that photoelectron events which nominally occur in the gap between anodes are, in general, detected in both adjacent channels. This effect, which is relatively insensitive to MCP gain, increases the effective spectral region sampled by each channel of the IPD.

Figure 4 shows data obtained during a pressure scan of the FPI through 2 Free Spectral Ranges. A frequency stabilized laser was used to provide a narrow spectral line and thus these data represent the interferometric instrument transfer function. The

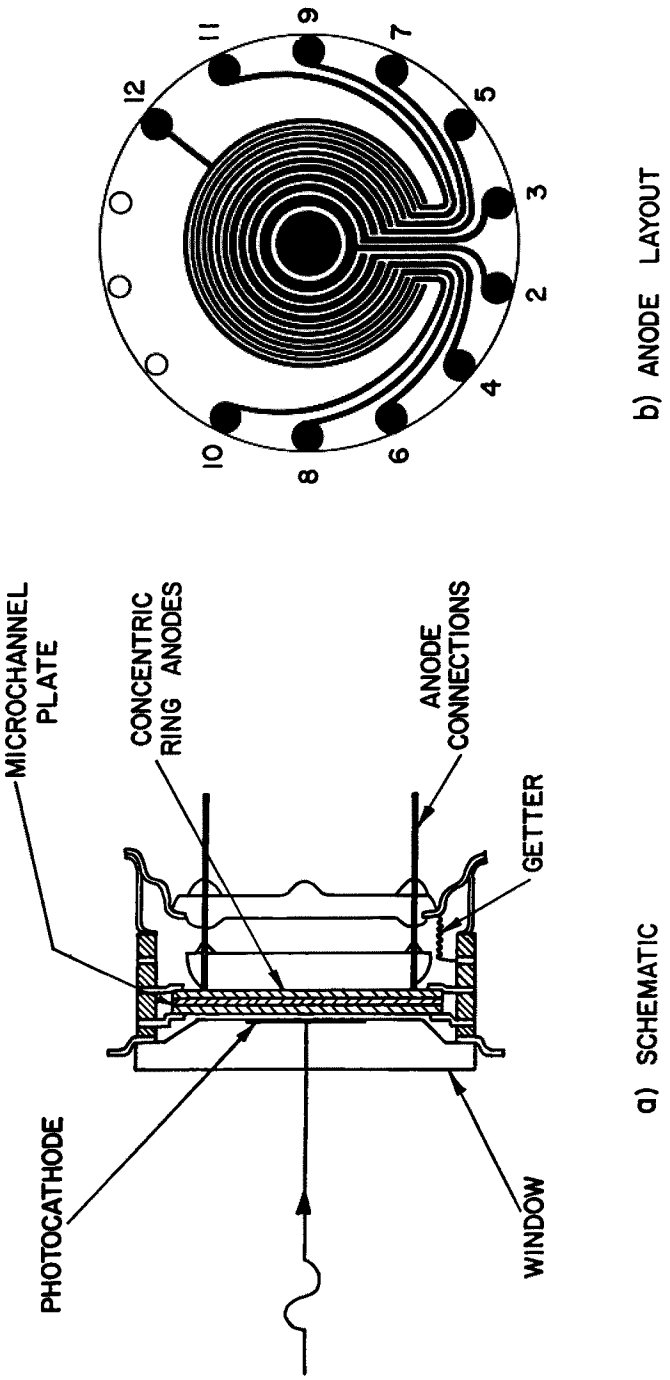

Fig. 3. Schematic diagram of the Image Plane Detector, (a) Internal structure, (b) Layout of multichannel anode.

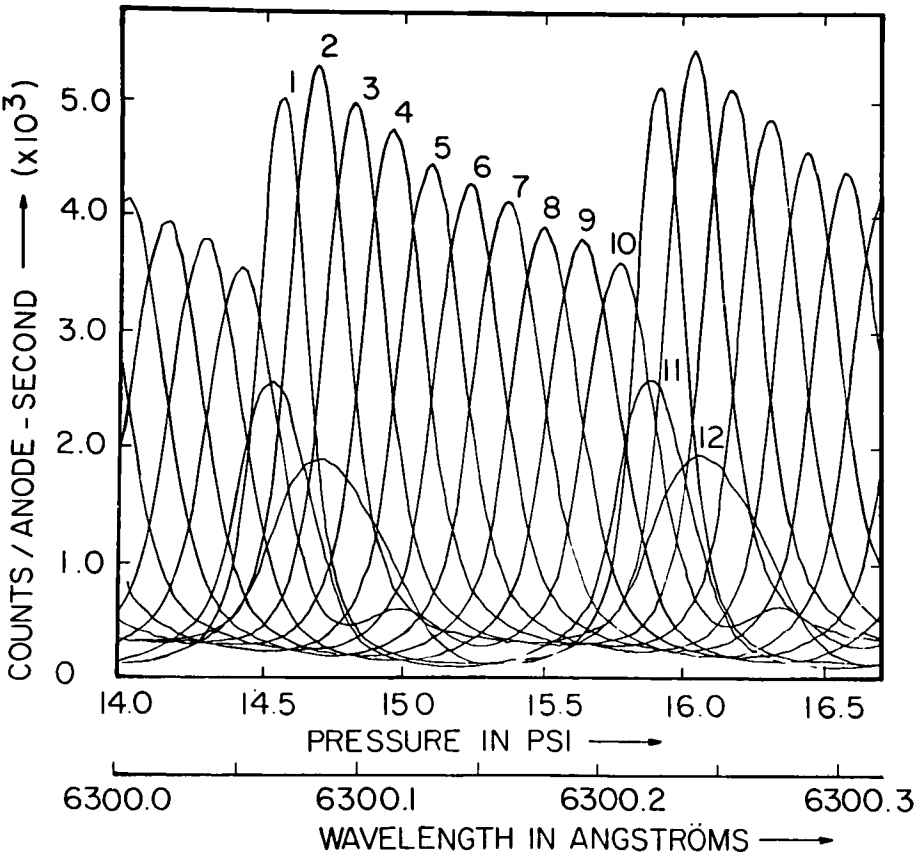

Fig. 4. Pressure scan data from the Fabry-Perot Interferometer. The interferometric transfer function for each channel is plotted with pressure (dry nitrogen) and wavelength. The data were obtained with a frequency stabilized laser source.

TABLE III

Anode geometry

Anode	Outside radius	Delta R cm
1	0.173	0.1730
2	0.245	0.0717
3	0.300	0.0550
4	0.346	0.0464
5	0.387	0.0409
6	0.424	0.0370
7	0.458	0.0340
8	0.490	0.0316
9	0.520	0.0299
10	0.548	0.0281
11	0.574	0.0267
12	0.600	0.0255

Area of anode ring: 0.0942 cm^2

decrease in finesse with increasing channel number is principally due to the offaxis optical aberrations. The relatively low sensitivities of channels 11 and 12 are due to the imperfect masking of the photocathode and the collection of photoelectron events occurring outside the metalized region of the anode respectively. The secondary peak seen in the channel 10 response is due to the detection of the next higher order fringe; this is also due to imperfect masking. Since the instrument function is characterized by a Fourier series and not by a idealized analytic function, these defects do not severely decrease the measurement accuracy.

The first MCP in the stack has a thin surface film of AlO deposited to protect the photocathode from bombardment by backstreaming ions [6]. A series of life tests carried out on several backup IPD's indicates that the useful working life of the flight device exceeds 0.1 C/cm^{-2} total processed output charge. This is in excess of 2 yr in orbit with the instrument operating at a 30% duty cycle.

2.5. Electronics and Modes of Operation

The electronic system designed to meet the FPI instrument requirements is illustrated in Figure 5. The Galactic Background Monitor (GBM), described in an appendix to this paper, shares the primary command and telemetry formatting systems. The IPD is protected from exposure to very bright sources by a 'squint' mechanism similar to that flown on Atmosphere Explorer. In this system, the bias voltage on the IPD cathode is reversed when the count rate exceeds a threshold. For further information the reader is referred to [1].

The Fabry-Perot interferometer can be commanded into a number of discrete operational modes. The most useful of these modes are listed below; several modes designed as engineering monitors and for failure contingency planning are not included.

(A) Filter Wheel

(1) Fixed filter: any one of eight possible filter positions.
(2) Filter cycling: the filter wheel may be stepped at the following rates: (a) once per $2^n * 0.5$ s (n = 0–7) in fast (default) mode; (b) once per $2^n * 0.5$ s (n = 3–7) in slow (backup) mode.
(3) Filter sequencing: the filter wheel may be commanded to alternate between any two filter positions.
(4) Impulsive go step (automatic filter sequence) if logic is lost.

(B) Scan Mirror

(1) Fixed mirror: any one of 16 sky positions and 2 calibration positions.
(2) Scan mirror cycling: the mirror may be stepped once per $(2^n * 0.25) + 0.25$ s (n = 0–7).
(3) Impulsive go step (automatic scan sequence) if logic is lost.

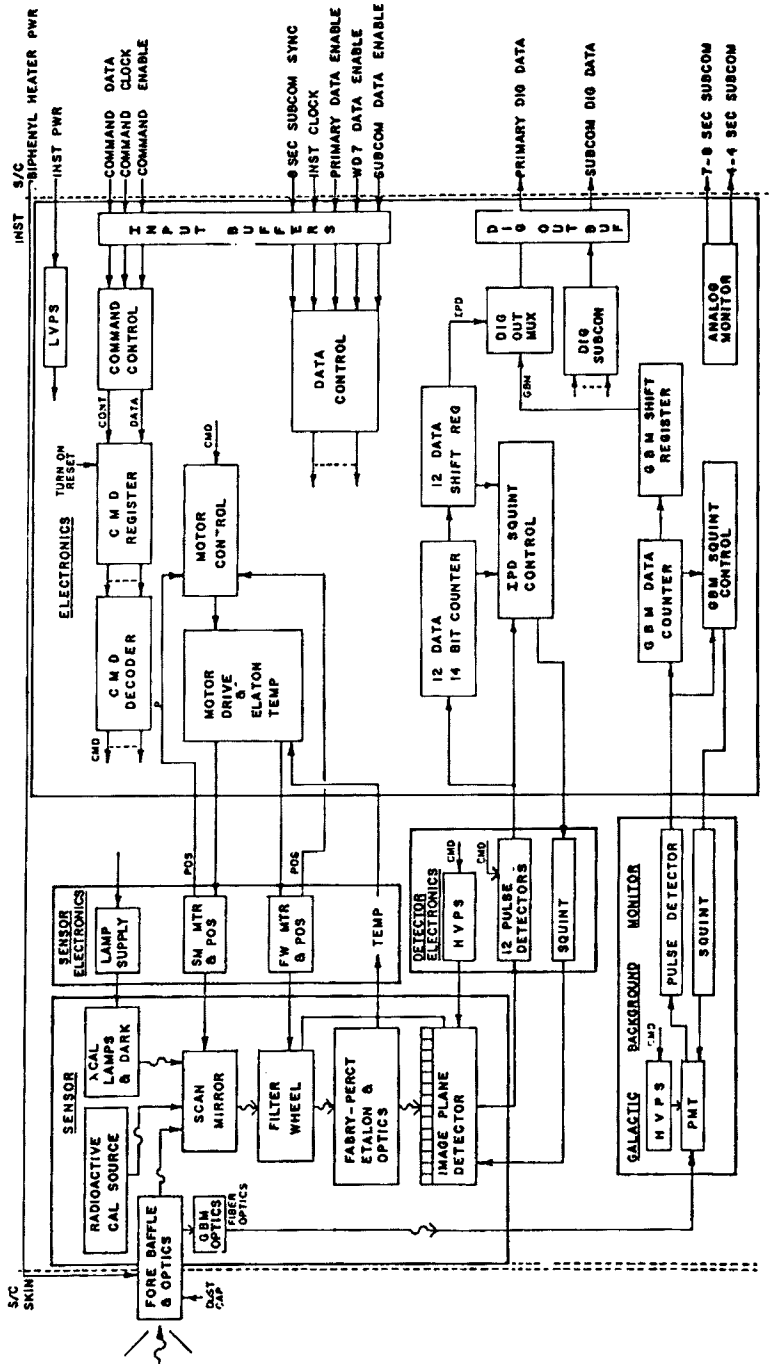

Fig. 5. Electronic system block diagram.

(C) Detector High Voltage
  (1) Nominal state (electron gain: 10^6).
  (2) High voltage increased in steps of 100 V to a possible maximum of (nominal + 800) V.
  (3) High voltage decreased in steps of 100 V to a possible minimum of (nominal − 700) V.

(D) Gain Measurement
  (1) Discriminator nominal state.
  (2) Discriminator cycling from nominal to high.

(E) Calibration Lamps
  (1) Selected lamp on and timed.
  (2) Selected lamp on continuously.
  (3) Selected lamp off.

The fixed filter, fixed mirror modes will be principally employed to view dim emissions such as the N(^{2}D) 5200 Å line and nightglow thermospheric lines. The fixed filter, scanning mirror modes will be used to obtain vertical profiles of thermospheric temperatures and winds; the scan rate being determined by the surface brightness of the emission feature and the required precision of the measurement. A useful mode will involve alternating the filter wheel between the O^+(^{2}P) 7320 Å emission and the neutral O(^{1}D) emission at 6300 Å. This mode will enable an investigation of the coupling between the neutral and ionic components of the thermosphere in the same temporal and spatial region.

3. Data Analysis

3.1. Nature of the Data

Figure 6 illustrates the form of the first level of scientific data from the FPI. In this spectrogram, the output of the instrument has been simulated for typical dayside thermospheric conditions (6300 Å) by convolving a Gaussian source function with the measured instrument transfer function. Analysis of such a spectrogram yields the geophysical parameters; wind, temperature, surface brightness and continuum brightness. The spectrograms also contain information on the state of thermalization of the emitting species.

3.2. Data Reduction

We have chosen, for the purposes of data reduction, to characterize the instrument transfer function at each wavelength by a Fourier series. The coefficients of this series are calculated from laboratory calibration data such as shown in Figure 4. The response of the instrument to a uniform source can be written:

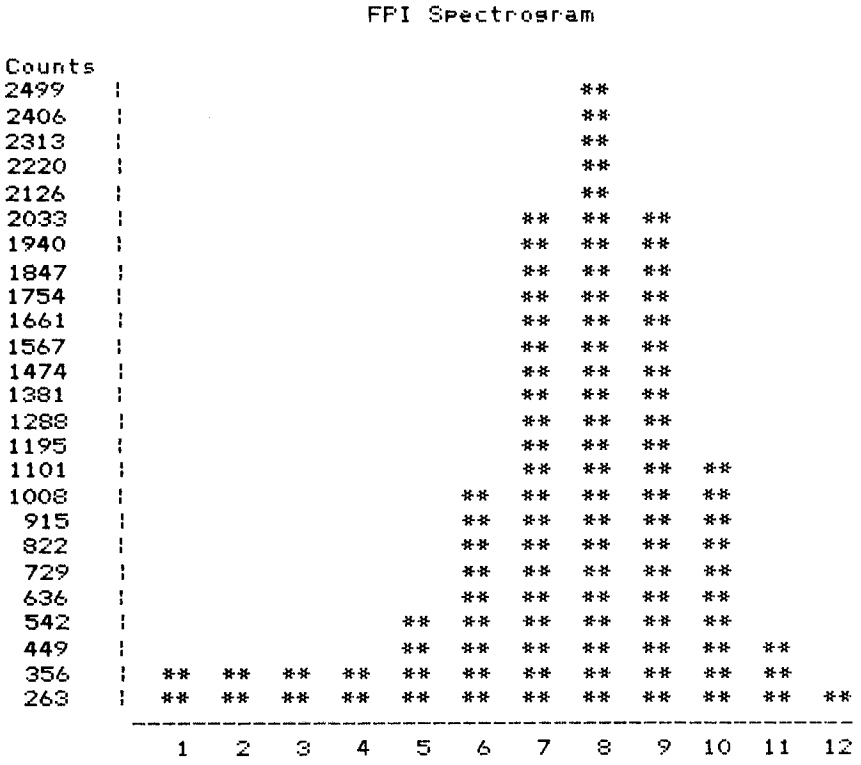

PEAK ANALYSIS Integration time : 1.00 sec

Iteration	Wind m/s	Temp. K	Bright R	Contin. R/A
	283.	200.		
1	228.8	657.	9258.	108.20
2	198.5	932.	9867.	43.22
3	194.1	987.	9970.	31.12
4	194.0	989.	9973.	30.80
5	194.0	989.	9973.	30.80
ERRORS:	15.7	70.	179.	16.32

Fig. 6. Spectrogram output from FPI showing the form of a typical thermospheric 6300 Å measurement. The data have been analyzed using an iterative matrix multiplication technique (see text). The errors shown represent 1 standard deviation for each observable. The units for the brightness and continuum brightness are Rayleighs and Rayleighs per Angstrom respectively.

$$N_j = C_{0j}t\left\{\overline{\Delta\lambda}_F \frac{\partial R}{\partial\lambda} A_{0j}\left(\frac{1-R_e}{1+R_e}\right) + \right.$$
$$+ T_F(\lambda_l) R_l\left[A_{0_j} + \sum_{n=1}^{\infty}\left(A_{nj}\cos\frac{2\pi n}{L}(\lambda_l - \lambda_F) + \right.\right. \quad (1)$$
$$\left.\left. + B_{nj}\sin\frac{2\pi n}{L}(\lambda_l - \lambda_F)\right) e^{-n^2G^2}\right]\Bigg\} + N_j \text{ dark}$$

with

$$C_{0j} = \frac{N_{j\text{cal}}}{A_{0j}\overline{\Delta\lambda}_F \left.\frac{\partial R}{\partial\lambda}\right|_{\text{cal}} t_{\text{cal}}}\left(\frac{1+R_e}{1-R_e}\right)$$

$$G = \frac{\pi\lambda_l}{Lc}\left(\frac{2kT}{m}\right)^{1/2}$$

and

$$\lambda_l = \lambda_0\left(1 + \frac{u}{c}\right).$$

In this formulism, N_j is the count recorded in channel j for an integration period t, C_{0j} is the sensitivity of channel j in counts per Rayleigh per second, $\overline{\Delta\lambda}_F$ is the filter integral width in Å, $\partial R/\partial\lambda$ is the continuum brightness in Rayleighs per Å. $T_F(\lambda_l)$ is the filter transmission at the wavelength of the doppler shifted emission line λ_l, R_l is the surface brightness of the emission line in Rayleighs, T is the temperature in deg Kelvin, A_{nj} and B_{nj} are the Fourier series coefficients normalized such that $A_{01} = 1.0$, L is the Free Spectral Range in Å, λ_F the reference wavelength for the Fourier series, R_e the etalon reflectivity. $\partial R/\partial\lambda\,|_{\text{cal}}$ and $N_{j\text{cal}}$ are the screen spectral brightness and counts detected in a period t_{cal} respectively for a white light laboratory calibration, k is Boltzmann's constant, m is the mass of the emitting specie. The relative velocity between the spacecraft and the emission region is given by u, and c is the velocity of light. λ_0 is the zero velocity center wavelength of the emission line. N_j dark is the detector dark count.

The four unknowns, u, T, R_l, and $\partial R/\partial\lambda$ may be calculated from the measured spectrogram using a nonlinear least squares fitting technique. However, to conserve limited ground data system resources, we linearize the problem by expanding Equation (1) about empirically determined approximations (u_0, T_0) for the wind and the temperature using only first order terms in the expansion. In this manner, the geophysical parameters may be obtained by a single matrix multiplication operation.

$$x_k = \sum C_{kj} N_j \qquad \text{with} \quad k = 1\text{–}4 \quad (2)$$

where

$$x_1 = R_l$$

$$x_2 = R_l(u - u_0)$$

$$x_3 = R_l(T - T_0)$$

$$x_4 = \partial R/\partial\lambda$$

The degree of precision obtained depends on the proximity of the input values for wind and temperature to the actual values. The numerical data of Figure 6 illustrates the rate of convergence of this matrix technique for a typical thermospheric spectrogram starting from rather poor input values for the temperature and wind. Five iterations are shown; the matrix calculated in each case is based on the results of the previous iteration. We will reduce computation time for the reduction of FPI data by storing a comprehensive set of pre-calculated matrices in the ground based computer memory. The most suitable matrix for an individual spectrogram will be selected automatically by a simple algorithm which provides approximate values for the temperature and wind.

3.3. Inversion techniques

The spatial information obtained by the FPI instrument during any view on the horizon contains contributions from all altitudes above the tangent ray height. The basic data we obtain are brightnesses as a function of wavelength and tangent ray height. These data can be Abel inverted to obtain volume emission rates versus height for a spherically symmetric atmosphere [7], or tomographically inverted [8, 9] for a non spherically symmetric atmosphere. However, this process will inject noise into the final deduced winds and temperatures. We have found an approximation which weights the doppler width and shift of each observed spectrogram with the brightness of the overlying airglow to assign a wind and temperature to a specific tangent ray height. The general theory of this weighting will be discussed in a more theoretical paper; for the present it is sufficient to note that the wind and temperature perturbation at a given height is given by the expression

$$Y_k(r_e) = \int \left[\overline{Y}_k(r)\, W_1(r, r_e) + \frac{\partial \overline{Y}(r)}{\partial r}\, W_2(r, r_e) \right] \mathrm{d}r \tag{3}$$

where

$$Y_1(r_e) = u(r_e)$$

$$Y_2(r_e) = T(r_e) - T^{(0)}$$

and $\overline{Y}_k(r)$ is the apparent value of the kth parameter obtained from the raw spectrogram. For the simple case of an exponential airglow layer this expression simplifies to the following series

$$Y_k(r_e) = \overline{Y}_k(r_e) - \frac{H_0}{2}\frac{\partial \overline{Y}_k(r_e)}{\partial r} - \frac{H_0^2}{3}\frac{\partial^2 \overline{Y}_k(r_e)}{\partial r^2} + \ldots$$

where the volume emission rate of the emission feature is given by

$$\eta(r) = \eta_0 e^{-(r - r_0/H_0)}.$$

The method described above is of course much more flexible than we have outlined here, but this example will serve to illustrate the technique.

4. Sensitivity and Accuracy

4.1. Calibration and Numerical Sensitivity

The absolute instrument sensitivity is dependent on the transmission of the optics and filters as well as on the instrument geometry and the photon-counting efficiency of the detector. The sensitivities for channel 1 of the IPD at the various wavelengths are listed in Table IV. The sensitivities of the remaining IPD channels are all within 35% of these values.

TABLE IV

Instrument sensitivities

Wavelength (Å)	Sensitivity (cnts $R^{-1} s^{-1}$)
5200	0.215
5577	0.201
5896	0.142
6300	0.098
7320	0.050

The units used are counts detected per Rayleigh in 1 s integration time period. The standard lamp used for these measurements is a tungsten ribbon lamp bearing a National Bureau of Standards calibration. We believe that our absolute calibration is correct to within 20%.

4.2. Analysis of Errors

The accuracy of any given measurement is governed by the accuracy of the instrument calibration and the counting statistics. The line-of-sight weighted standard deviations are simply derived in the matrix formulism viz:

$$\overline{(\delta x_k^2)}^{1/2} = \left(\sum (C_{kj})^2 N_j \right)^{1/2}$$

where

$\overline{(\delta x_k^2)}^{1/2}$ is the standard deviation on the measurement of x_k.

Figure 7 shows the standard deviations for temperature and wind at 6300 Å calculated for various surface brightness conditions and for various integration time periods.

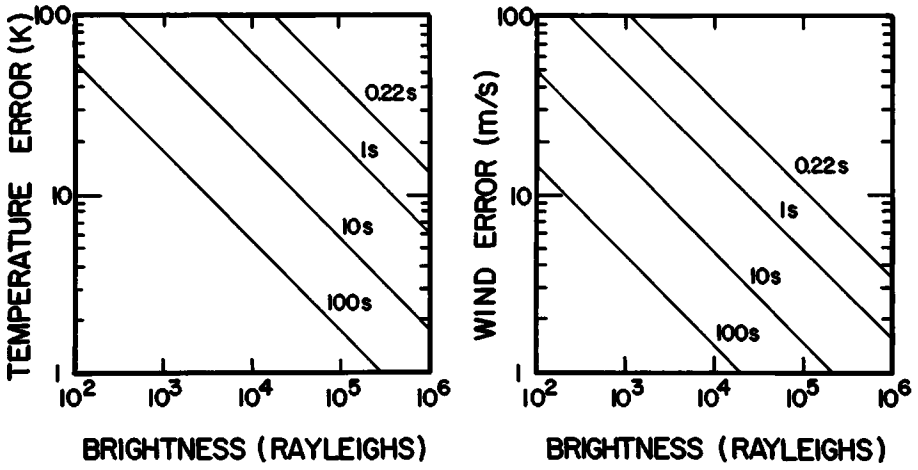

Fig. 7. Statistical errors for the measurement of wind and temperature as functions of surface brightness calculated for several different integration time periods. Errors shown are for thermospheric measurements at 6300 Å.

Acknowledgements

The authors would like to express gratitude for the engineering assistance of W. H. Hansen and M. E. Dobbs and for the programming support from R. J. Theriault. We would also like to thank David Rees of University College London for invaluable discussions and for providing and testing flight quality etalons. We wish to point out that the GBM and its data analysis were developed cooperatively by the University of Michigan and the University of Texas at Dallas. W. B. Hanson and N. W. Spencer have contributed by their helpful remarks. This work was supported by NASA under grant number NAS5–24296.

Appendix A

The Galactic Background Monitor

Early concern over the influence of galactic point sources on the spectrum obtained from the Fabry-Perot interferometer led us to append to our instrument an optical star track monitor. It soon became apparent that with slight modification this device could assist in determining the orientation of the spacecraft. This modified device will be briefly described in this appendix.

(a) *Optics*

The Galactic Background Monitor (GBM) is a simple two axis broadband photometer which contains at its infinity focus a digital encoder mask. One optical axis of the GBM is parallel to the spacecraft X-axis, the other inclined at 30 deg toward the $-Z$ spacecraft

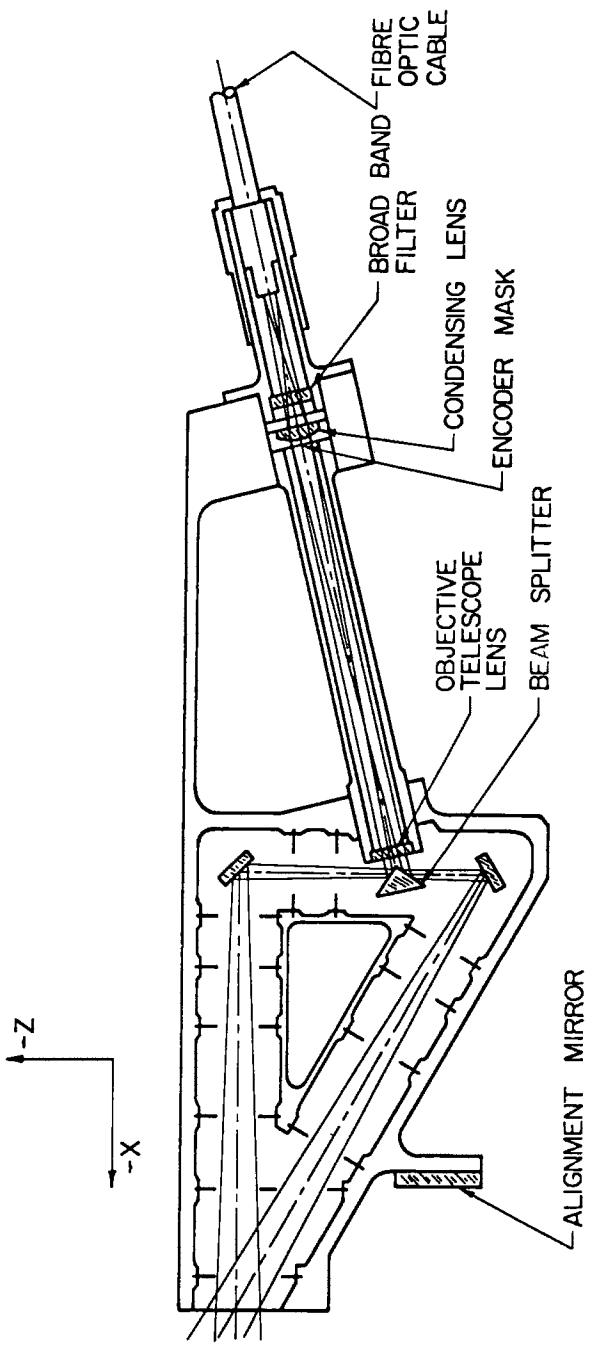

Fig. 8. Optical schematic for the Galactic Background Monitor.

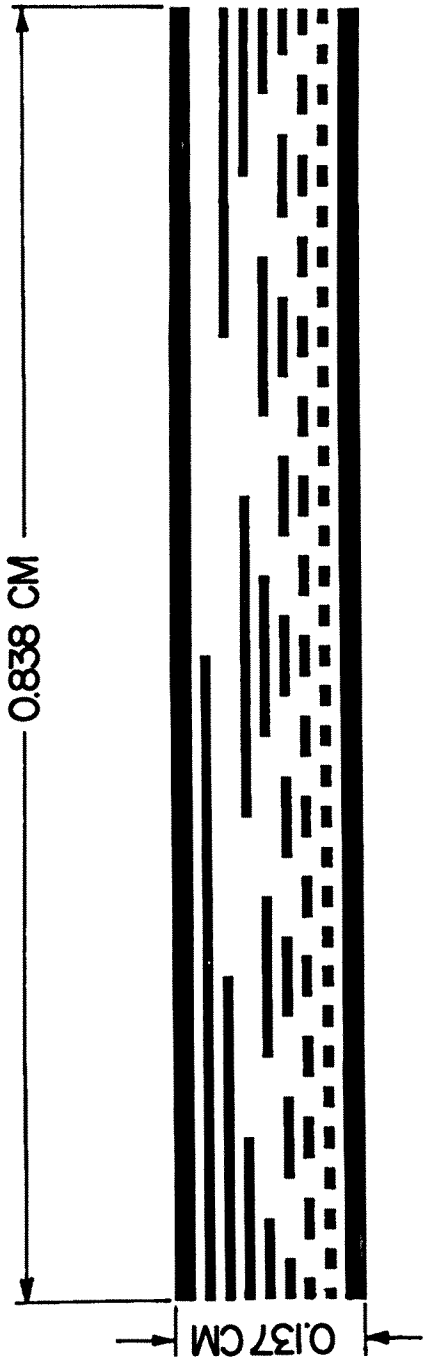

Fig. 9. Binary focal plane mask for the Galactic Background Monitor.

axis in the X-Z plane. The light coming from both axes is summed on the encoder plane allowing a single photomultiplier to detect stars within either of the two fields of view. These characteristics are illustrated in Figure 8. We note that light pasing through the encoder mask is filtered by a simple high pass blocker made of 1 cm of SF6 G5 radiation resistant glass. This filtered signal is then conducted by a quartz fibre optics cable to a photomultiplier tube and electronics which are identical to the detector system of the Atmosphere Explorer Visible Airglow Photometer (VAE). The block diagram for the FPI electronics shows the GBM system in detail.

(b) *Star Signal*

The signal generated by a star depends upon the visual magnitude of the star and the transfer function of the GBM. Table AI lists the signal count calculated for this instrument. We note that 5th magnitude stars can be observed. The star image moves as the spacecraft axis traverses the sky. Thus, the star crosses the encoder mask, creating a unique binary pattern in time depending on the azimuth angle of the star. The least significant bit of the mask represents an angular separation of 0.03 deg. The mask is shown in Figure 9. It should be noted that the spacecraft pitch angle is determined at the time that the star enters or leaves the encoder identification bars.

TABLE V

Star magnitude	GBM signal count (t = 0.125 s)
−1	8243
0	3297
1	1319
2	528
3	210
4	84
5	33.8

The results of an orbit of GBM data are a set of star sightings in two ribbons 3 deg wide in the sky. One ribbon is centered in the orbital plane and the other on a cone of full angle 120 deg about the orbit normal. These data uniquely determine the spacecraft angular orientation within 0.03 deg at each star crossing. These results will be used to correct the spacecraft attitude in order that the instruments measuring velocity have a stable baseline known to approximately ± 4 m s^{-1}.

References

1. Hays, P. B., Carignan, G. R., Kennedy, B. C., Shepherd, G. G., and Walker, J. C. G.: *Radio Sci.* **8**, 369 (1973).
2. Mayr, H. G., Harris, I., and Spencer, N. W.: *Rev. Geophys. Space Phys.* **16**, 539 (1978).
3. Dickinson, R. E.: *Rev. Geophys. Space Phys.* **13**, 771 (1975).
4. Rishbeth, H.: *J. Atmos. Terr. Phys.* **34**, 1 (1972).

5. Hays, P. B., Meriwether, J. W., and Roble, R. G.: *J. Geophys. Res.* **84**, 1905 (1979).
6. Csorba, I. P.: *Appl. Opt.* **18**, 2440 (1979).
7. Hays, P. B. and Roble, R. G.: *Planet. Space Sci.* **16**, 1197 (1968).
8. Cormack, A.: *J. Appl. Phys.* **34**, 2722 (1964).
9. Fesen, C. L.: Ph.D. Thesis, University of Michigan (1981).